https://doi.org/10.1595/205651323X16686891950941 *Johnson Matthey Technol. Rev.*, 2023, **67**, (1), 47–59

JOHNSON MATTHEY
TECHNOLOGY REVIEW

technology.matthey.com

X-Ray Computed Tomography for Failure Mechanism Characterisation within Layered Pouch Cells: Part II

Post-mortem analysis of failed cells

Drasti Patel, Hamish Reid
Electrochemical Innovation Lab, Department of Chemical Engineering, University College London, Torrington Place, London, WC1E 7JE, UK

Sarah Ball$
Johnson Matthey, 142A Park Drive, Milton Park, Abingdon, OX14 4SE, UK

Dan J. L. Brett, Paul R. Shearing*
Electrochemical Innovation Lab, Department of Chemical Engineering, University College London, Torrington Place, London, WC1E 7JE, UK; The Faraday Institution, Quad One, Becquerel Avenue, Harwell Campus, Didcot, OX11 0RA, UK

Email: *p.shearing@ucl.ac.uk;
**sarah.ball@evmetalsgroup.co.uk

$Present address: EV Metals UK Ltd, 142A Park Drive, Milton Park, Abingdon, Oxfordshire, OX14 4SE, UK

PEER REVIEWED

Submitted 28th February 2022; Revised 8th July 2022; Accepted 2nd August 2022; Online 3rd August 2022

In Part I (1), the failure response of a 1 Ah layered pouch cell with a commercially available nickel manganese cobalt (NMC) cathode and graphite anode at 100% state of charge (SOC) (4.2 V) was investigated for two failure mechanisms: thermal and mechanical. The architectural changes to the whole-cell and deformations of the electrode layers are analysed after failure for both mechanisms. A methodology for post-mortem cell disassembly and sample preparation is proposed and demonstrated to effectively analyse the changes to the electrode surfaces, bulk microstructures and particle morphologies. Furthermore, insights into critical architectural weak points in LIB pouch cells, electrode behaviours and particle cracking are provided using invasive and non-invasive X-ray computed tomography techniques. The findings in this work demonstrate methods by which LIB failure can be investigated and assessed.

1. Results and Discussion

This section contains a comprehensive discussion of a post-mortem analysis using X-ray computed tomography (CT) and scanning electron microscopy (SEM) techniques, and is categorised according to the type of analysis: whole-cell and component.

1.1 Whole Cell Investigation

The whole cell analyses were carried out using the 'non-invasive' sample preparation technique. The cells pre- and post-failure were examined at two spatial resolutions as shown in **Figure 1**. The first set, using the Nikon XT H 225 X-ray macro-CT instrument (Nikon Metrology, Japan) achieved voxel sizes of 31.7 μm, 33.6 μm and 27.8 μm for the pristine cell (Cell 1), thermally failed (Cell 2) and the nail penetrated (Cell 3), respectively. The second set, using the ZEISS Xradia 520 Versa X-ray micro-CT instrument (ZEISS, Germany) with a 4x objective lens (region-of-interest (ROI) scan with *ca.* 3–4 mm field of view), achieved voxel sizes of 1.83 μm, 2 μm and 1.7 μm for Cell 1–3, respectively. For the larger voxel size scans, the architecture of the whole cell, i.e. the outer casing of the pouch, the tabs and the electrode layers (anode and cathode) are distinguishable based on their grayscale values. As a result, the behaviour of these features when subjected to different trigger mechanisms can be compared.

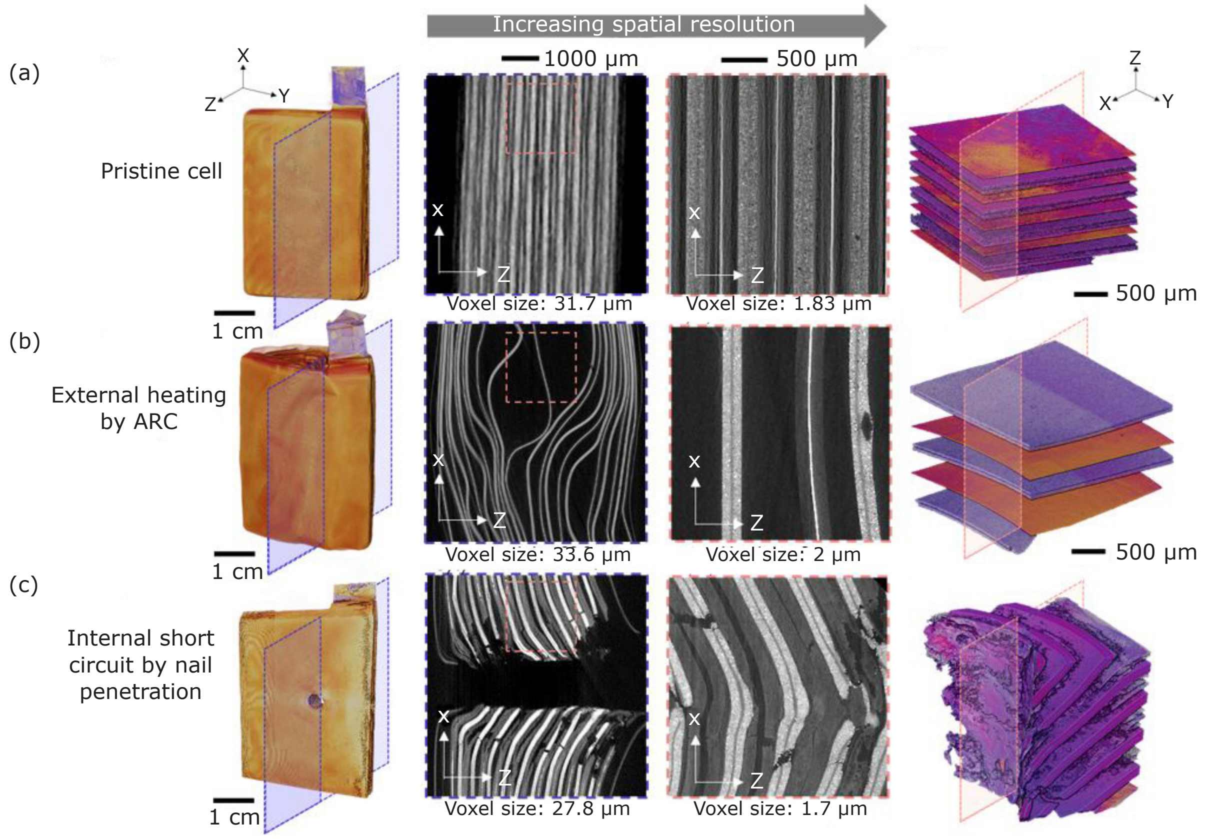

Fig. 1. Volume renderings and orthogonal slices in the XZ planes for: (a) the pristine cell (Cell 1); (b) the thermally failed cell (Cell 2); and (c) the nail penetrated cell (Cell 3), respectively. Corresponding scan numbers are 1–6 in Table S2 in the Supplementary Information

For example, the outer casing and disorder in electrode layers in Cell 2 reveal that there was a greater pressure build-up and distribution within the thermally failed cell compared to that of the nail penetrated cell (Cell 3). The microstructure of the electrode layers also reveals where cracks formed and how they differ between the two types of failure. For the nail penetrated cell, the largest and most prominent cracks are all distributed directly above or below the nail, whereas cracks in the thermally failed cell are distributed across the whole cell architecture, but are concentrated in areas where kinks have occurred in the electrode layers due to large gas pockets. A more comprehensive analysis of the two failure types and comparisons with the pristine cell is reported in the following sections.

1.1.1 Thermal Failure: External Heating by Accelerating Rate Calorimetry

Increased reactivity due to external heating in lithium-ion batteries (LIBs) is often a consequence of solid electrolyte interphase (SEI) decomposition and exposure of the anode to the electrolyte causing self-heating reactions. When this heat is not well dissipated, the temperature of the cell continues to rise due to sustained exothermic reactions (often denoted the 'acceleration' stage). Further reactions involving electrolyte oxidation at the cathode surface eventually cause the cell to enter the thermal runaway stage. During this stage, several high-rate electrode reactions will continue to generate heat, and the cell may eventually catch fire and rupture. A typical self-heating rate used to characterise thermal runaway of a lithium-ion cell is 10°C min^{-1} or higher. Thermal runaway temperatures can vary between 130°C to 200°C or greater and are highly dependent on cell size, format and materials. From **Figure 2(a)**, it appears that Cell 2 did not reach thermal runaway (i.e. a self-heating rate >10°C min^{-1}), however, visual inspection suggests significant thermal damage by fire (charring of outer case). The temperature profile in **Figure 2(a)** reveals that the self-heating rate between 60°C and 130°C remains below 1°C min^{-1}. The decomposition of SEI is typically expected to begin at 60°C, exposing the anode surface to the reactive electrolyte.

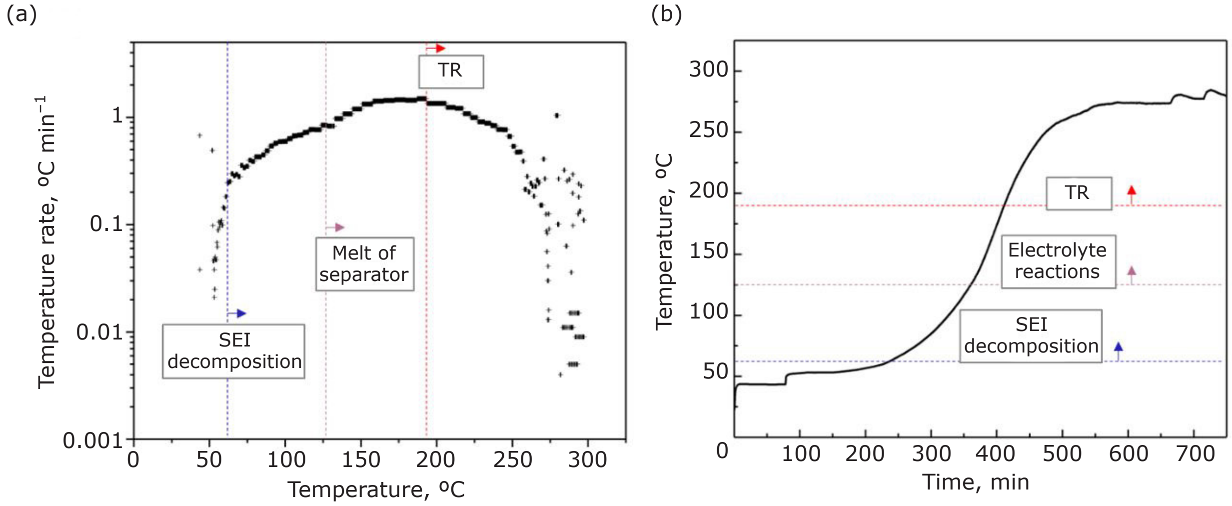

Fig. 2. Accelerating rate calorimetry (ARC) self-heating rate profiles of a 1 Ah layered pouch cell. A start temperature of 50ºC was increased stepwise by 5ºC: (a) the inflection at *ca*. 125ºC shows the start of an increase in heat generation above 1ºC min^{-1}; (b) this can be seen in the curve before the plateau in the self-heating profile. At this temperature, it can be assumed that this attributes to the breakdown of the SEI layer

Exothermic reactions between the two are expected to occur at *ca*. 100°C. Heat generation from this promotes an elevation of the cell temperature. The inflection at *ca*. 125°C may be a result of the separator melting since the self-heating rate shortly after this reaches the >1°C min^{-1} region. Shortly after the separator melts, short circuits between the aluminium and copper current collectors may have caused a high local rate of Ohmic heat generation, as shown by the continuing rise in temperature in **Figure 2(a)** and **2(b)**. After this point, decomposition of the anode is expected to continue and as the temperature nears 200°C, the decomposition of the electrolyte, binders and cathode materials may also occur. However, in this test, the self-heating rate drops below 1°C min^{-1} at *ca*. 175°C, this is suspected to be a result of the thermocouple detaching from the cell.

While the temperature profiles begin to provide a dynamic, thermomechanical understanding of the phenomena occurring within the pouch cell during thermal failure, there is limited understanding of the mechanical dynamics: such as how heat and gas generated from the SEI decomposition dissipate through the cell or areas where short circuits may have occurred. **Figure 3(b)** shows a three-dimensional (3D) image of the whole cell after thermal failure. The swelling of the outer pouch can be seen along with the dislocated electrode layers. The orthoslice views in the XZ and ZY planes offer an insight into the build-up of gas and the distribution of pressure within the cell. Orthoslice (position **A**) in the XZ plane (**Figure 3(a)**) shows two distinct gaps where generated gas may have escaped through the vacuum seal vertically along the length of the cell. Orthoslice (position **C**) in the XZ plane reveals that there is a significantly larger space between the central (or 10th) layers vertically along the length of the cell; however this is not the case in the perpendicular direction which has an uneven displacement across all the layers as shown in **Figure 3(c)** in orthoslice (position **G**). It is evident that venting of the cell also occurs across the seals close to the tabs from orthoslice (position **E**) in the ZY plane, as expected since this is mechanically the weakest point of the cell architecture. As there were no internal temperature measurements taken, it is difficult to predict the temperature distribution across the cell. However, a comparable pouch cell that underwent thermal runaway in literature suggests that the temperature distribution within a cell of this format is characteristically uneven and can result in a longer failure duration and more gradual mechanical expansion (2) when compared to a cylindrical cell for example (3). The distribution of melted materials (such as aluminium or copper) within a cell during failure often indicates internal cell temperatures; for example, Finegan *et al*. report that molten aluminium remnants enhanced the heat dissipation of local exothermic reactions. For Cell 2, however, there are no visible globules of aluminium in the obtained X-ray CT images, suggesting the internal cell temperatures did not exceed the melting point of aluminium (>660°C).

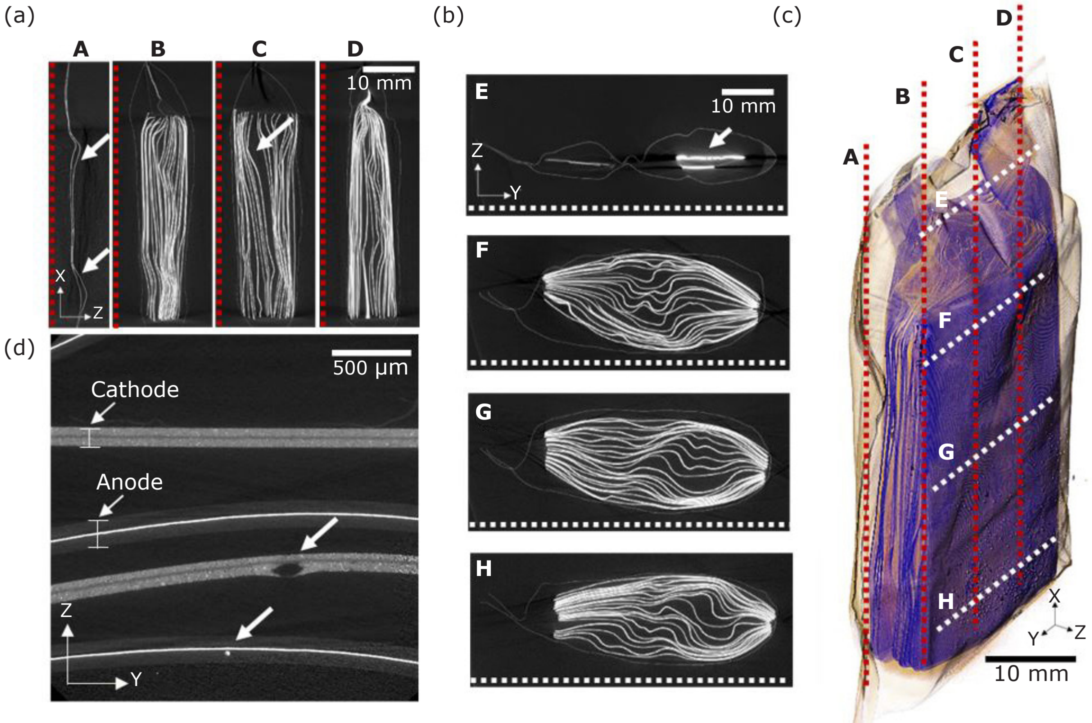

Fig. 3. Images of pouch cell after thermal failure (Cell 2). Images from the whole cell X-ray CT scan in orthoslices along the: (a) XZ planes; and (b) ZY planes show the electrode architecture after deformation due to gas generation. The swelling of the outer casing is visible in (b) in the **E**, **F**, **G** and **H** positions (voxel size: 33.6 µm). The welded anode tab appears to be detached in (b) position **E** (where the bright white areas are the copper current collector and nickel tab). A volume rendering in (c) shows the electrode layer architecture within the swollen outer casing, and (d) the orthoslice in the ZY plane with a voxel size of 2 µm, shows defects in the cathode and anode layers. Corresponding scan numbers are 2 and 5 in Table S2 in the Supplementary Information

The two-dimensional (2D) orthoslice at a higher spatial resolution in **Figure 3(d)**, although limited by the field of view (3 mm), reveals the undisturbed electrode layer architecture in greater detail. In the two cathode and two anode layers visible, there does not seem to be significant delamination of the active cathode or anode layer from their respective current collectors (aluminium and copper). Although the image is taken at the centre of the cell, it is difficult to deduce with confidence which layer number it is in reference to the whole stack (20 layers). The defect highlighted in the cathode active layer is suspected to be due to a small defect from the cathode fabrication rather than as a result of the thermal failure. As expected, the separator layer is not visible as it had melted.

1.1.2 Nail Penetration: Internal Short Circuit Failure

Nail penetration can severely damage the internal components of the LIB. Metallic current collectors and separators with insufficient flexibility can fracture and cause direct contact between electrodes. As a result, heat is often generated after a localised short circuit and if the rate of heat dissipation is less than the rate of generation, thermal runaway may be initiated. The centre of Cell 3 was pierced by a nail during the test (100% nail depth). It is believed that a large amount of heat may have generated local to the nail tip and the electrolyte may have decomposed shortly after the short circuit: firstly, from the heat generated, and secondly, from reacting with the oxygen entering through the rupture. The gas generation is predicted to have only lasted a short amount of time, and no thermal runaway occurred. The cell did not catch fire as recorded in the video available in the Supplementary Information with the online version of this article, and the photograph of the cell outer casing in Figure 3(b) in Part I (1) shows how the cell casing appears intact, aside from the point of nail ingress.

Figure 4(b) shows X-ray CT images of the 1 Ah pouch cell after nail penetration and **Figure 4(a)** shows the pristine, un-failed cell for comparison. From the orthoslice in the XZ plane of the whole cell scan in **Figure 4(e)**, it is evident that all layers were affected by the nail penetration event as a

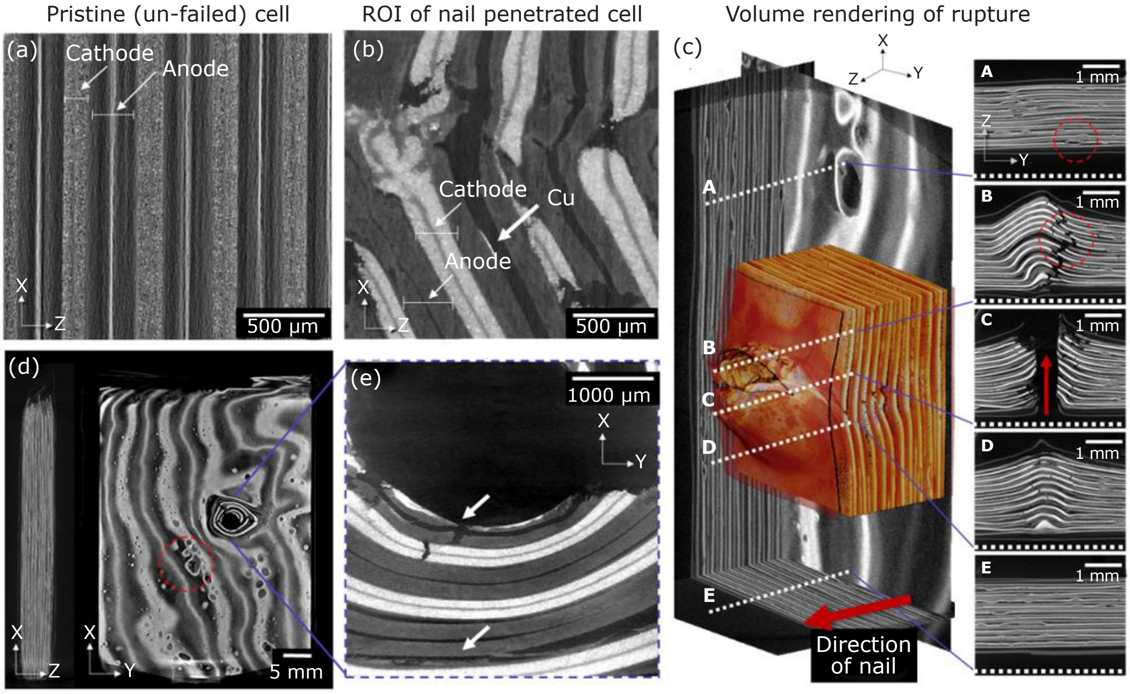

Pristine (un-failed) cell

ROI of nail penetrated cell

Volume rendering of rupture

Fig. 4. (a) Orthoslice of the pristine cell (Cell 1) in the XZ plane (voxel size: 1.83 μm); and (b)–(e) orthoslice of the nail penetrated cell (Cell 3) in various planes. The direction of the nail is highlighted in (c) where a volume rendering of the rupture is shown. Corresponding scan numbers are 3, 4 and 6 in Table S2 in the Supplementary Information.

result of the distribution of gas generation across the cell. A closer inspection in **Figure 4(d)** reveals delamination of the cathode active material from the aluminium current collector across the whole cell, and at a greater degree concentrated near the point of nail ingress (positions **A–E**). The high specific heat and thermal conductivity of aluminium may have enhanced the dissipation of the heat generated from the electrolyte reactions. Fractures and cracks are also visible in the microstructure of the bulk electrode layers. When compared with the thermally failed cell (Cell 2), the estimated pressure (or disruption of electrode layers) within the nail penetrated cell is significantly smaller.

A combination of multiple failure behaviours is visible in the ROI scans with voxel size 1.7 μm (**Figure 4(b)**): the shear stress crossing multiple layers, fracture and breaking of current collectors and dislodging of electrode particles. Under tension, the electrodes' mechanical response is dominated by the property of the current collector (4). Furthermore, weak points caused by the intrusion of the active particles into the metal foil as a result of calendaring lower the tensile failure strain of the current collector (5). In the orthoslice in the XZ plane in **Figure 4(b)**, and XY plane in **Figure 4(f)**, (i.e. looking through the rupture in the direction of the nail), delamination of the anode material (graphite) from the copper current collector is visible. The copper current collector also appears to have disintegrated near the rupture. In some areas, the heated copper likely reacted with oxygen from the surrounding air entering the cell and produced copper oxide (as can be seen in the green areas highlighted in the photographs of the cell after failure in Figure S3 in the Supplementary Information). The greyscale value of a material is dependent on its X-ray absorption coefficient. Highly attenuating materials are brighter and whiter, such as copper, and those with lower attenuation coefficients, such as aluminium, are darker. There is little contrast between the greyscale values of copper and copper oxide owing to their similar densities (8.96 g cm^{-3} and 6.0 g cm^{-3}); as a result, it is difficult to distinguish this from the orthoslices in **Figure 4(b)**. Furthermore, copper or copper oxide is only visible in small portions of the rupture.

The heat response of a nail penetration-induced short circuit event was not measured in this work, however, it is assumed that the temperature of the whole cell did not increase above 120°C, the melting point of the polyethylene separator, as it was still intact after cell-opening.

A volume rendering of the rupture and its corresponding orthoslices (in positions **A–E**) in **Figure 4(c)** and **4(d)**, respectively, show where breaks occurred. The rupture developed in both the transverse and nail direction, resembling the shape of a cross, as predicted by Sahraei *et al*. (5). Directly above the nail (in position **B**), a transverse fracture, vertically along the length of the cell, and the across all the layers is visible. Areas, where the current collectors have folded, can also be seen (i.e. where multiple short circuits may have occurred). It is not well known how the evolving microstructural fractures, cracks and folds influence the heat distribution leading up to and during the thermal runaway process.

Electrode particles near the rupture centre are severely dislodged which may also have contributed to the short circuit failure. However, it is difficult to confidently conclude whether this was a result of the nail entering (during failure) or leaving the cell (after failure).

1.2 Cell Opening: Component Investigation

1.2.1 Bulk Electrode Layer

After opening the cells, the cathode, anode and separator were carefully separated (Figure 3 in Part I (1)). From the samples harvested from the thermally failed cell, both the anode and cathode displayed a non-homogeneous surface with some distinct deterioration as seen in Figure 3 **B** and **C** in Part I (1). Large, dark areas appear on the cathode surface primarily where the surface was still in contact with the anode surface. At temperatures greater than 120°C, the SEI, binder materials and separator are expected to have melted (6). This is likely to be the reason why the cathode active layer was easily detached from the aluminium current collector during handling. The anode material in Figure 3(a) **B** in Part I (1), in some regions, is detached from the copper current collector. Some darker areas on the surface are primarily due to the detachment of the material from the cathode following its degradation under high temperatures. For the samples taken from the nail penetrated cell (Figure 3(b) **E** and **F** in Part I (1)), there are some stark differences in the macroscopic appearance of the electrode surfaces: both surfaces have traces of the separator which melted in some areas. The cathode surface has some distinct features: the surface is rough, and areas where gas pockets formed causing the active material from the aluminium current collector to delaminate are visible. Furthermore, the surface appears homogeneous in colour, compared to the thermally failed cathode, and it was easier to handle (no flaking). The anode layer in comparison displayed a non-homogeneous surface with some silver-grey areas possibly indicating lithium plating. In the areas close to the rupture (or hole left from the nail penetration), sections, where the copper has oxidised, are visible in green. Darker regions are areas which are expected to be a result of some of the graphite layer being attached to the separator.

Figure 5 shows the SEM images of the pristine (**Figure 5(a)** and **(d)**), thermally failed (**Figure 5(b)**) and nail penetrated (**Figure 5(c)**) cathode materials as well as the thermally failed (**Figure 5(e)**) and nail penetrated (**Figure 5(f)**) anode materials. The cathode material of the pristine cell (**Figure 5(a)**) displays a uniform morphology with some dispersed binder, cracks and secondary particles. As seen in **Figure 5(d)**, the secondary particle is a spherical agglomerate constructed from primary particles. For the thermally failed cell, some microscopic features display areas where fragments from the melted separator and products from the electrolyte decomposition (i.e. $LiPF_6$, LiF, PF_5) have accumulated (7). In comparison to the pristine cathode, there are fewer cracked particles. It is expected that temperatures above 175°C would have resulted in the breakdown of the active cathode material (8), and the propagation of degradation may have occurred more due to the larger surface area than through particles with no visible microcracks (9). The microscopic appearance of the cathode surface after nail penetration in **Figure 5(c)** on the other hand appears unchanged when compared to the pristine cathode. This is further explored (for the nail penetrated cell) in Figure S8 in the Supplementary Information, where SEM images were taken from the top, middle and bottom samples of the central cathode layer to investigate the representativeness of the observed surface morphology. The appearance of the surface remains mostly uniform regardless of location, though the middle image (closest to the nail and rupture) appears to have a greater number of interparticle voids, likely a result of gas expansion.

Figure 5(e) and **5(f)** show the morphology of the anode materials after thermal failure and nail penetration, respectively. After the breakdown of the SEI layer on the anode surface the exposed intercalated lithium reacts with the electrolyte solution. A thick deposited layer morphology and cracking of the layer is visible for the thermally failed anode; a single anode particle boundary cannot be distinguished through the layer which is predicted to be caused as a result

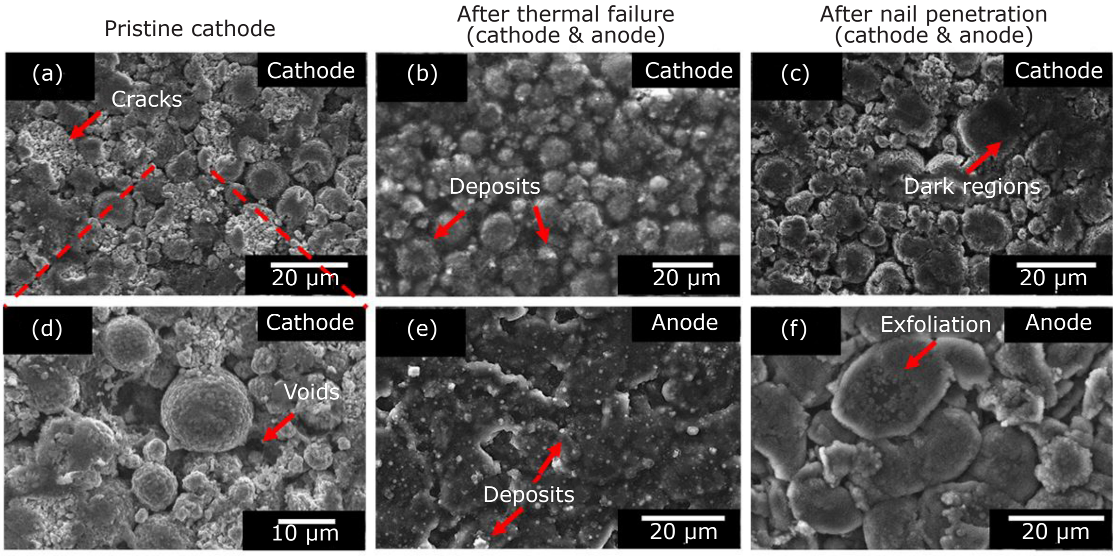

Fig. 5. SEM micrographs of: (a) the pristine cathode at 3050 magnification; (b) the cathode after thermal failure at approximately 3000 magnification; (c) cathode after nail penetration at approximately 3500 magnification; (d) the pristine cathode at 4720 magnification; (e) anode after thermal failure at approximately 3000 magnification; and (f) anode after nail penetration at approximately 3500 magnification.

of the decomposition reactions occurring at temperatures above 150°C (10). While images of the pristine anode were not collected in this work, comparisons with a pristine graphite anode surface in literature (11, 12) demonstrate how the surface of the anode after nail penetration remains relatively intact with regards to the appearance of clear boundaries. However, the particle surface displays some evidence of degradation or exfoliation which could be explained by the breakdown of the SEI at high temperatures causing new graphitic edges and plane fragments to be exposed at the surface.

Overall, the SEM images reveal important microscopic and surface level changes to the bulk electrode layers. While collecting the images is a relatively fast method and can cover a large area across the electrode surface, there are still several features, specifically delamination of the cathode and anode layers from their respective current collectors and microstructural parameters such as particle size distribution (PSD) that are difficult to quantify from 2D images alone. The following section reports the findings from a 3D analysis of the bulk electrode layers using X-ray micro-CT.

The thermally failed and nail penetrated cells, Cells 2 and 3 respectively, were opened and samples of the anode and cathode electrode layers (0.4 mm x 0.4 mm square) were extracted. **Figure 6** shows orthoslices in the XY and XZ planes and their corresponding volume renderings from X-ray micro-CT scans. A visual comparison between the two cathodes (thermally failed and nail penetrated) reveals that there is no significant change to the bulk electrode structure. Further comparison with the pristine cathode bulk layer in Figure S4 in the Supplementary Information confirms there is little difference (at this resolution) from the fresh state to the failed. Anode samples from both cells follow the same trend.

The PSD of the pristine cathode sample is compared to that of the post-mortem samples: thermally failed (Cell 2) and nail penetrated (Cell 3). Table S2 in the Supplementary Information summarises the PSD findings, as well as the particle volume fraction, tortuosity factor and surface area per volume extracted from the datasets. The mean diameter extracted from the pristine bulk cathode layer is 5.39 μm, and the mean diameters for the samples extracted from Cells 2 and 3 were 4.76 μm and 6.10 μm, respectively. It is difficult to confidently conclude a trend from the mean particle diameters extracted from the bulk electrode layers due to the limited resolution of the X-ray technique and the small sample size. However, the spread of data in the PSD (Figure S5 (a)–(c) in the Supplementary Information) shows there is an additional peak below 2.5 μm for both the failed cathode layers when compared to the pristine cathode. This is predicted to be a result of debris, fractured surface particles or delamination of particles from the

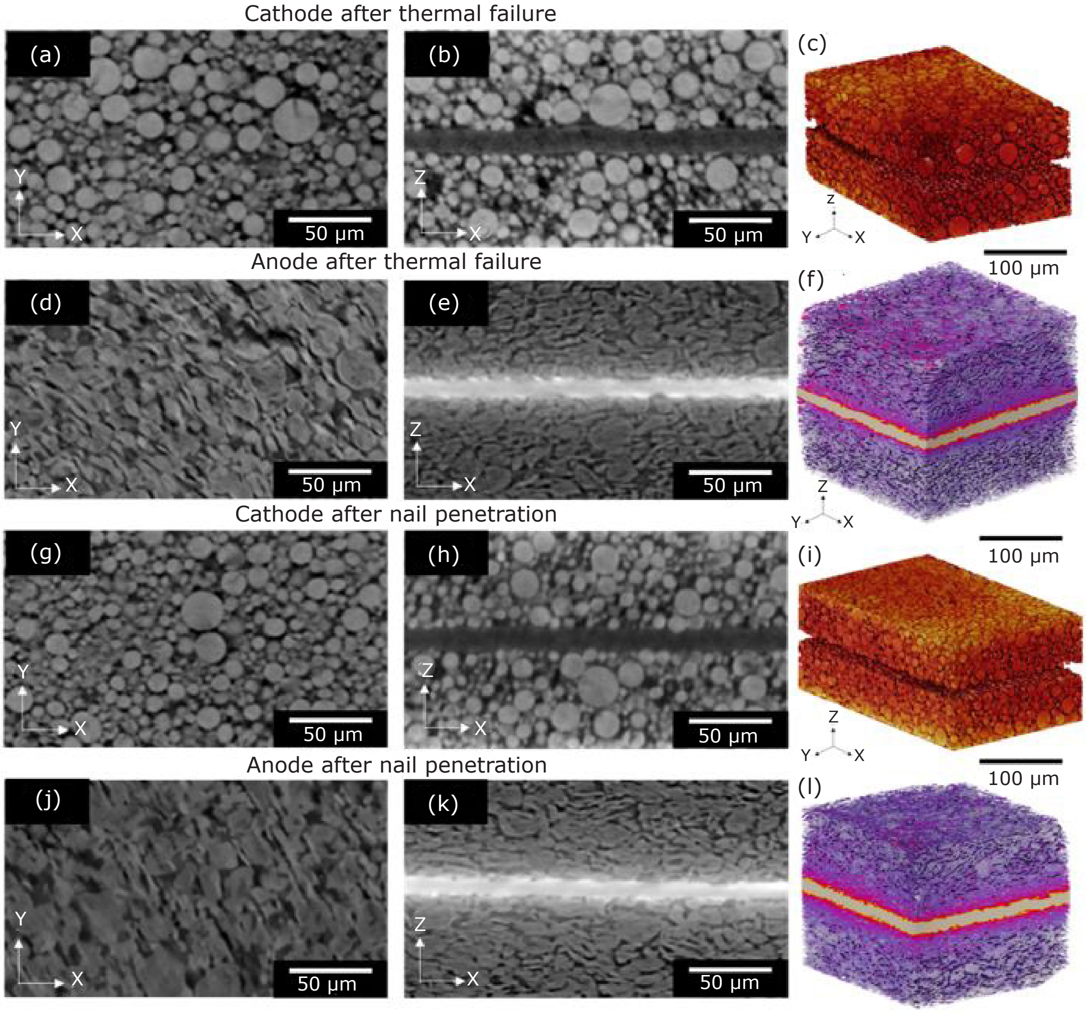

Fig. 6. Orthoslices in the XY and XZ planes, and volume renderings, of: (a)–(c) cathode and (d)–(f) anode after thermal failure; (g)–(i) cathode and (j)–(l) anode after nail penetration. Corresponding scan numbers are 8–11 in Table S2 in the Supplementary Information.

aluminium current collector. **Figure 8** shows the percentage change of parameters extracted from the bulk cathode layers of Cell 2 (thermal failure) and Cell 3 (nail penetration) from the pristine bulk cathode layer.

There are a greater number of particles with a diameter <1 µm in the thermally failed cathode layer compared with the nail penetrated sample. This is not reflected in the particle volume fractions and the surface area per volume for the three samples (Table S2 in the Supplementary Information), which are, in the same order, 0.46, 0.40 and 0.48, and 0.478, 0.408, 0.490. The particles that underwent thermal failure (and reached temperatures >250°C) exhibit the lowest surface area per volume, which contradicts what is expected: the smaller the particle size, the lower the thermal stability of the material (13). The temperature profile of the nail penetrated cell (Cell 3) was not measured, however, from literature (14, 15), it is predicted that the temperature of the nail tip for this cell type may have exceeded 120°C and initiated localised heat generation: causing the electrolyte to boil and generate gas (6).

The bulk anode layer from Cell 2 has a greater mean particle diameter, 16.99 µm than the sample from Cell 3, 13.59 µm. However, the pore volume fraction (0.31 and 0.36), surface area per volume (0.654 and 0.660) and tortuosity factor (2.97 and 3.19), of the thermally failed and nail penetrated anodes are similar. The surfaces of the two anodes in **Figure 5(e)** and **5(f)** show the structure of the effects of heating to temperatures >250°C and the extent of decomposition and deposits on the surface of the thermally failed anode. However, the 3D analysis shows how the anode and its microstructural properties remained intact below the surface. This is reflected in the spread of data of the PSD (Figure S6 (a)–(b) in the Supplementary Information) where there are a greater number of particles with diameters >25 μm for the thermally failed anode, which is expected to be those furthest away from the current collector and shown in the 2D surface images.

From the whole cell scans, there were obvious areas where the cathode and anode layers had delaminated from their respective current collectors. However, due to the small sample size (0.4 mm x 0.4 mm) required for the bulk electrode layer scans, it is difficult to directly observe this phenomenon. Furthermore, despite using the whole cell scans to predict where to extract samples; it was still difficult to pinpoint an area where delamination had occurred. Bulk electrode layer scans are useful for determining key material characteristics such as PSDs and tortuosity. They are especially useful for understanding heat distribution across layers within a whole cell, however, they are limited by their sample size and may not give a full representation of the phenomena that occurred during failure.

1.2.2 Electrode Particles

Figure 7(a) shows the cathode in its pristine state at a voxel resolution of 0.0631 μm, in the XZ plane. Similarly, **Figure 7(b)** and **7(c)** show the cathode extracted from the thermally failed and nail penetrated cells, at voxel resolutions of 0.126 μm. All three samples clearly show two phases: particle (light grey) and pore and carbon binder domain (dark grey). It is difficult to distinguish between the pore and carbon and binder domain at this resolution (16). The mean particle diameters are 2.93 μm (pristine), 4.43 μm (thermally failed) and 4.47 μm (nail penetrated). When compared to the Versa datasets, the pristine cathode has an unexpectedly small mean particle diameter in comparison to that extracted from the pristine bulk cathode layer (5.39 μm). This may have a direct correlation to the number of

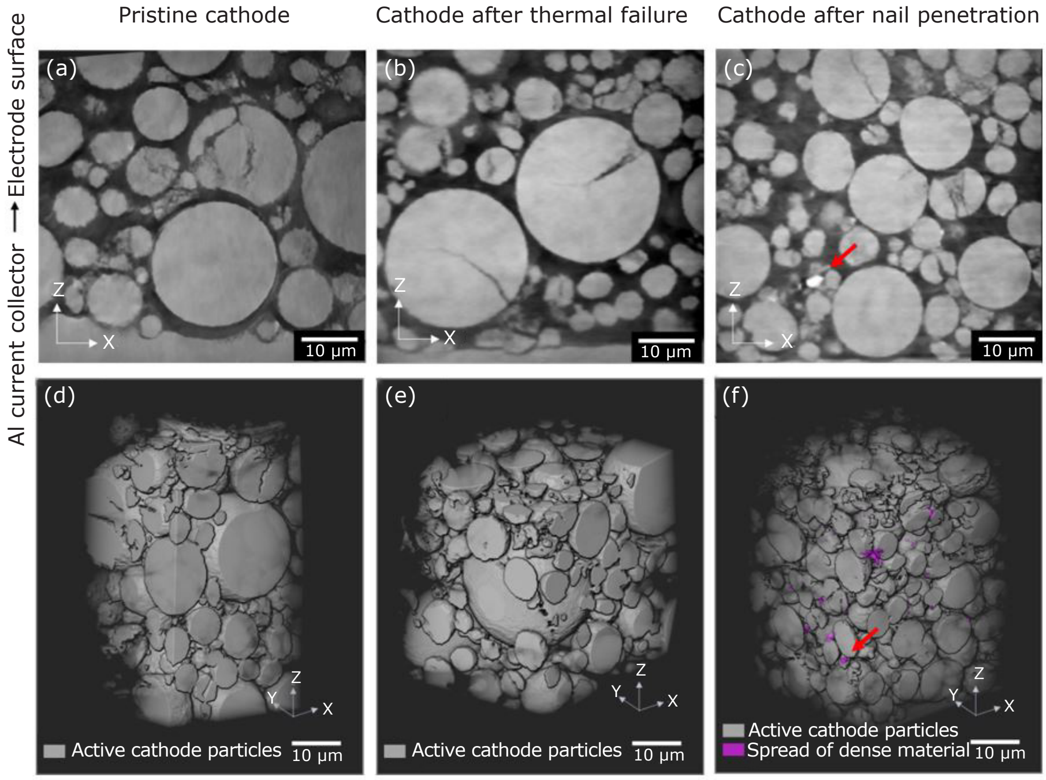

Fig. 7. Orthoslices in the XZ plane of the cathode acquired using X-ray nano-CT for: (a) pristine; (b) after thermal failure (Cell 2); and (c) after nail penetration (Cell 3) samples. The aluminium current collector is at the bottom (visible in (a) and (b)) and the electrode surface is at the top. A highly attenuating spot is highlighted in (c); volume renderings of: (d) pristine, (e) Cell 2 and (f) Cell 3 show the particles after segmentation. The denser material deposits are highlighted by the red arrow. Corresponding scan numbers are 12–14 in Table S2 in the Supplementary Information.

intraparticle cracks within the pristine sample. For example, the label analysis carried out during the PSD extraction may have assigned a single particle that was cracked in two as two separate particles with smaller diameters. As a result, the greater the number of particle cracks; the greater the number of smaller particle sizes in the PSD (17). **Figure 8** highlights the extent of variation of the parameters extracted from the bulk electrode layer (micro-) and particle morphology (nano-CT) 3D images. The surface area per volume of the post-failure cathode particles showed the greatest increase when compared to the surface area per volume of the pristine particles. This could be attributed to the changes in the particle morphology and orientation within the cathode layer as a result of the failure mechanisms (18, 19). Nevertheless, it is still important to consider the sample volume and its statistical significance here, while this resolution helps elucidate certain particle features, it is difficult to confidently compare the PSD trends obtained from the bulk electrode layers that have greater sample sizes/bounding box dimensions (see Table S2 in the Supplementary Information). A representative volume analysis of the particle scans shown in Figure S7 in the Supplementary Information however illustrates the accuracy of the pore volume fraction and tortuosity factors across the sample sizes for Ultra scans (<65 μm).

The particles within the cathode layer after nail penetration display some bright regions, highlighted in the greyscale image in **Figure 7(c)**. The brighter regions represent a highly attenuating and dense material such as cobalt or copper due to their high atomic masses. **Figure 4(b)** displayed dislodging of electrode particles, however, it is difficult to predict the precise cause of the contamination in *ex situ*. Typically, when a cell is forced to over-discharge, the cell voltage drops below the safe cut-off voltage. The nail penetration event is expected to have caused a localised internal short circuit and triggered similar mechanisms to that of an over-discharge (20): rapid delithiation of the anode and lithiation of the cathode. As the anode potential increases, it can overcome the overpotential required for copper dissolution, as a result, copper is oxidised. Cu^{+}/Cu^{2+} ions may penetrate the separator and become deposited on the cathode surface. A volume rendering in **Figure 7(f)** shows the spread of the dense material within the cathode layer (acquired using X-ray nano-CT). The volume fraction of the dense material is 0.00028, making it difficult to distinguish in the SEM (**Figure 5(c)**) or micro-CT (**Figure 6 (g)**–**(l)**) images.

There are several microcracks, which do not span the entire particle diameter, and shattered particles, which present as small fragments across all three cathode samples (pristine, thermally

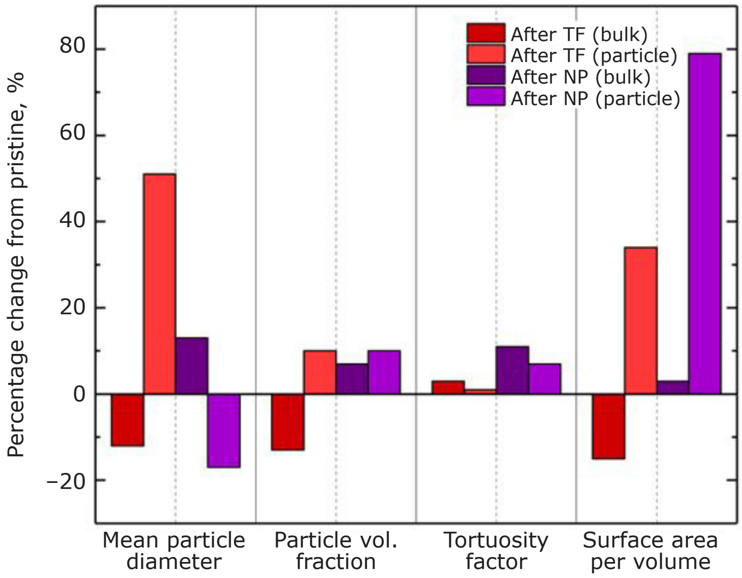

Fig. 8. Percentage change for the mean particle diameter, particle volume fraction, tortuosity factor and surface area per volume, of the micro-CT bulk electrode layer image (bulk), and nano-CT image (particle) of the thermally failed (TF) and nail penetrated (NP) cathode layers, from the pristine cathode layer and particle scans. A positive percentage represents an increase, and a negative represents a decrease. Corresponding scan numbers are 7, 9, 11–14 in Table S2 in the Supplementary Information.

failed and nail penetrated). It is predicted that the presence of these cracks is more likely to be a result of the manufacturing process (*via* calendaring) (9) than as a result of thermal or short circuit failure. Furthermore, **Figure 7(a–b)** shows areas where the active particles have intruded into the aluminium foil as a result of calendaring, suggesting that the local stress concentrations (21) were high enough to deform the current collector sheet, and subsequently high enough to induce microcracks and particle shattering.

2. Conclusion

Although LIBs are a suitable choice for the future of energy storage, concerns regarding their safety impede their widespread use in some sectors. LIBs can fail by multiple different failure mechanisms across their multi-layered structures and scales. While they're extensively investigated and tested at a whole and particle scale, there is limited standardisation across the methodologies for safety testing and post-mortem analyses. In this work, we present an outline for the use of X-ray CT to investigate failure mechanisms by invasive and non-invasive methods.

At present, whole-cell X-ray CT is used to investigate the architecture of a battery post-failure concerning its electrode deformation and safety features. Oftentimes it is used as a technique to determine specific areas of interest, for example, dendrite growth, electrode folds and tab placement. This work showcased the benefits of ROI scans at voxel resolutions between 1.7–2 μm in post-mortem cells. The whole cell X-ray CT in this work offered a method to investigate the volume change due to swelling, gas dispersion and bulk electrode behaviour from various stresses (heat and gas generation and puncture with a nail) within the cells without disturbing their delicate environments.

While invasive measurements yielded useful bulk electrode layer and particle parameters, they did not demonstrate a full representation of the failure phenomena. The post-mortem analysis by SEM is a relatively faster analysis method, however conclusions made solely from 2D images gave only a surface level understanding and key features such as particle mixing and electrode delamination were difficult to identify. X-ray micro- and nano-CT of the bulk electrode layer and particle morphologies were more useful for understanding the particle behaviour as a whole, for example, PSDs and cracking and how they may have affected heat dissipation throughout the cell, however, they were also proven to be insufficiently representative and were limited by the size of the sample. Furthermore, the overall technique requires complex sample preparation techniques which can make it a relatively slow method for commercial post-mortem analyses. Of the two failure mechanisms, the thermally failed cell appeared to undergo a more severe failure. It reached a higher maximum temperature and had significantly more damage across various length scales from its whole cell architecture (swelling and distribution of gas), layers (melted separator) and electrode surfaces (deposits). The nail penetrated cell, on the other hand, was relatively less severe: the majority of its outer shell casing remained intact and heat dissipated through the cell more uniformly.

X-ray CT has proven to be a useful tool for LIB failure analysis. Its widespread deployment in commercial LIB failure testing and analysis has often been limited by accessibility in terms of the high cost of equipment and time taken per scan. However, this is quickly changing as new research efforts aim to take better advantage of their capabilities; for example by developing methods for optimal sample preparation and faster acquisition times. Furthermore, it is important to note that due to the limited number of repeat tests presented here, conclusions with high confidence cannot be drawn from these results. Nevertheless, these results demonstrate the use of non-invasive X-ray CT for evaluating the effects of thermal and internal short circuit failures on the materials within LIBs, and this workflow, now established, can be readily applied to parametric studies of battery failure.

Acknowledgements

This work was supported by the Engineering and Physical Sciences Research Council (EPSRC), UK (EP/N032888/1, EP/R020973/1, EP/K005030/1, EP/M028100/1). Drasti Patel acknowledges funding from the EPSRC CASE Award scheme with Johnson Matthey. Paul Shearing acknowledges the support of The Royal Academy of Engineering (CiET1718/59) and The Faraday Institution (EP/S003053/1), grant number FIRG025 and FIRG028.

References

1. D. Patel, H. Reid, S. Ball, D. J. L. Brett and Paul R. Shearing, *Johnson Matthey Technol. Rev.*, 2023, **67**, (1), 36

2. M. T. M. Pham, J. J. Darst, D. P. Finegan, J. B. Robinson, T. M. M. Heenan, M. D. R. Kok, F. Iacoviello, R. Owen, W. Q. Walker, O. V. Magdysyuk, T. Connolley, E. Darcy, G. Hinds, D. J. L. Brett and P. R. Shearing, *J. Power Sources*, 2020, **470**, 228039
3. J. B. Robinson, J. A. Darr, D. S. Eastwood, G. Hinds, P. D. Lee, P. R. Shearing, O. O. Taiwo and D. J. L. Brett, *J. Power Sources*, 2014, **252**, 51
4. C. Zhang, J. Xu, L. Cao, Z. Wu and S. Santhanagopalan, *J. Power Sources*, 2017, **357**, 126
5. E. Sahraei, M. Kahn, J. Meier and T. Wierzbicki, *RSC Adv.*, 2015, **5**, (98), 80369
6. X. Feng, M. Fang, X. He, M. Ouyang, L. Lu, H. Wang and M. Zhang, *J. Power Sources*, 2014, **255**, 294
7. E. P. Roth and D. H. Doughty, *J. Power Sources*, 2004, **128**, (2), 308
8. Q. Wang, B. Mao, S. I. Stoliarov and J. Sun, *Prog. Energy Combust. Sci.*, 2019, **73**, 95
9. T. M. M. Heenan, A. Wade, C. Tan, J. E. Parker, D. Matras, A. S. Leach, J. B. Robinson, A. Llewellyn, A. Dimitrijevic, R. Jervis, P. D. Quinn, D. J. L. Brett and P. R. Shearing, *Adv. Energy Mater.*, 2020, **10**, (47), 2002655
10. D. P. Abraham, E. P. Roth, R. Kostecki, K. McCarthy, S. MacLaren and D. H. Doughty, *J. Power Sources*, 2006, **161**, (1), 648
11. B. Mao, H. Chen, Z. Cui, T. Wu and Q. Wang, *Int. J. Heat Mass Transfer*, 2018, **122,** 1103
12. W. Wu, R. Ma, J. Liu, M. Liu, W. Wang and Q. Wang, *Int. J. Heat Mass Transfer*, 2021, **170**, 121024
13. J. Geder, H. E. Hoster, A. Jossen, J. Garche and D. Y. W. Yu, *J. Power Sources*, 2014, **257**, 286
14. D. P. Finegan, B. Tjaden, T. M. M. Heenan, R. Jervis, M. Di Michiel, A. Rack, G. Hinds, D. J. L. Brett and P. R. Shearing, *J. Electrochem. Soc*, 2017, **164**, (13), A3285
15. T. Yokoshima, D. Mukoyama, F. Maeda, T. Osaka, K. Takazawa, S. Egusa, S. Naoi, S. Ishikura and K. Yamamoto, *J. Power Sources*, 2018, **393**, 67
16. S. R. Daemi, C. Tan, T. Volkenandt, S. J. Cooper, A. Palacios-Padros, J. Cookson, D. J. L. Brett and P. R. Shearing, *ACS Appl. Energy Mater.*, 2018, **1**, (8), 3702
17. F. Röder, S. Sonntag, D. Schröder and U. Krewer, *Energy Technol.*, 2016, **4**, (12), 1588
18. O. O. Taiwo, D. P. Finegan, D. S. Eastwood, J. L. Fife, L. D. Brown, J. A. Darr, P. D. Lee, D. J. L. Brett and P. R. Shearing, *J. Microsc.*, 2016, **263**, (3), 280
19. X. Lu, A. Bertei, D. P. Finegan, C. Tan, S. R. Daemi, J. S. Weaving, K. B. O'Regan, T. M. M. Heenan, G. Hinds, E. Kendrick, D. J. L. Brett and P. R. Shearing, *Nat. Commun.*, 2020, **11**, 2079
20. G. Zhang, X. Wei, X. Tang, J. Zhu, S. Chen and H. Dai, *Renew. Sustain. Energy Rev.*, 2021, **141**, 110790
21. P.-C. Tsai, B. Wen, M. Wolfman, M.-J. Choe, M. S. Pan, L. Su, K. Thornton J. Cabana and Y.-M. Chiang, *Energy Environ. Sci.*, 2018, **11**, (4), 860

The Authors

Drasti Patel is a PhD researcher at the Electrochemical Innovation Lab (EIL) at University College London (UCL), UK. Her project is part sponsored by Johnson Matthey. Her research interests are in lithium-ion battery materials characterisation and failure assessment using X-ray CT imaging and calorimetry.

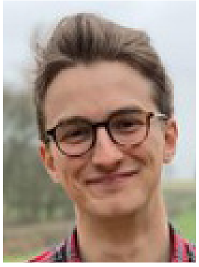

Hamish Reid is currently a PhD researcher at the EIL at UCL. Prior to joining the EIL, Hamish gained a Chemistry with a Year in Industry MChem at the University of Sheffield, UK, where he spent a year working at The Dow Chemical Company, USA. After graduating, Hamish worked at Faradion Ltd, UK, researching cathode and anode materials for rechargeable sodium-ion batteries. His current research interests include X-ray imaging, battery safety and degradation of high nickel content lithium-ion cathode materials. Hamish's doctorate work is partly funded by Johnson Matthey.

At the time of writing, Sarah Ball was Applications Technology Manager at Johnson Matthey. She has experience managing technical projects for lithium-ion batteries and hydrogen fuel cells, focusing on testing, evaluation and improvement of cathode and anode materials.

Dan Brett is a professor of Chemical Engineering at UCL. His research interests lie in electrochemical energy conversion and storage, electrochemical sensors; electroanalysis, hybrid vehicles and microgeneration technologies. He is also active in modelling, instrumentation development, engineering design, device fabrication, materials development and technoeconomic analysis of electrochemical energy conversion technologies.

Paul Shearing is a professor of Chemical Engineering at UCL and Royal Academy Engineering Chair in Emerging Battery technologies. His research interests lies in the design of electrochemical processes in devices including fuel cells, batteries and electrochemical reactors. He is involved in a wide range of projects which includes the understanding and development of batteries, fuel cells and other electrochemical processes and leads the LiSTAR project and the SAFEBATT project on battery safety, under the auspices of The Faraday Institution, UK.